High-Resolution Transmission Electron Microscopy Observation of Colloidal Nanocrystal Growth Mechanisms using Graphene Liquid Cells

Jong Min Yuk,[1,2,3]* Jungwon Park,[2,4]* Peter Ercius,[5] Kwanpyo Kim,[1,2,6] Danny J. Hellebusch,[2,4] Michael F. Crommie,[1,2,6] Jeong Yong Lee,[3]† A. Zettl,[1,2,6]† A. Paul Alivisatos[2,4]†

[1] Department of Physics, University of California at Berkeley, CA 94720, USA.

[2] Materials Sciences Division, Lawrence Berkeley National Laboratory, Berkeley, CA 94720, USA.

[3] Department of Materials Science and Engineering, KAIST, Daejeon, 305-701, Korea.

[4] Department of Chemistry, University of California at Berkeley, CA 94720, USA.

[5] National Center for Electron Microscopy, Lawrence Berkeley National Laboratory, Berkeley, CA 94720, USA.

[6] Center of Integrated Nanomechanical Systems, University of California at Berkeley, CA 94720, USA.

*These authors contributed equally to this paper.

†To whom correspondence should be addressed: j.y.lee@kaist.ac.kr; azettl@berkeley.edu; and alivis@berkeley.edu

Abstract

We introduce a new type of liquid cell for *in-situ* electron microscopy based upon entrapment of a liquid film between layers of graphene. We employ this cell to achieve high-resolution imaging of colloidal platinum nanocrystal growth. The ability to directly image and resolve critical steps at atomic resolution provides new insights into nanocrystal coalescence and reshaping during growth.

A wide range of physical, chemical, and biological phenomena that take place in liquids on the nanometer scale would benefit from observations with atomic resolution transmission electron microscopy. Yet it is only very recently that the powerful methods of electron microscopy have begun to be applied to imaging in liquids. Electron microscopy such as conventional transmission electron microscopy (CTEM), scanning transmission electron microscopy (STEM), and 4-D electron microscopy have long enabled direct observation of solid phase phenomena with atomic resolution (*1*-*4*). Applying these high-powered imaging tools to study liquid phase phenomena requires more consideration to maintain realistic conditions of the liquid specimen (*5*). For example, TEM requires high vacuum and uses a high-energy electron beam, which under certain conditions can be expected to induce rapid evaporation or damage to liquid samples. In early studies, these undesired effects were partially mitigated by environmental cells that contain a reservoir with a viewing window fabricated from Si_3N_4 or SiO_2 to mimic realistic liquid conditions during TEM observation (*6*-*8*). To date, these early liquid cells have enabled studies of nanoscale phenomena in liquids at resolutions of a few nm. Unfortunately, the relatively thick (tens to a hundred nm) and relatively high *Z* element windows in these specialized cells have poor electron transmittance, resulting in significant reduction of resolution and signal-to-noise ratio due to electron scattering, so that to date no liquid cell observations have been performed at atomic resolution.

An example of the benefits that could arise from atomic resolution in liquid cell studies arises in the growth of colloidal inorganic nanocrystals, such as Pt. The first movies of colloidal nanocrystal growth (*7*), restricted to lower resolution, revealed unexpected phenomena, namely that the colloidal Pt particles grow by frequent particle coalescence events, and most surprising, that the particle growth apparently pauses following a coalescence event. The reason for this apparent pause was attributed to possible structural rearrangements within the coalescing nanocrystals, but this conjecture could not be proven in the earlier studies.

Recently developed protocols for the high-yield fabrication of nanometer-thick suspended membranes such as graphene, graphene oxide, and boron nitride (*9-11*), have provided the ultimate transparent sample supports for electron microscopy (*12-15*). One carbon atom (Z=6) thick, graphene is the thinnest of these membranes. When used as a support for TEM specimens, graphene provides a high contrast for any type of material including isolated light atoms and organic molecules (*1, 16-17*). Moreover, it is straightforward to use graphene membranes to encapsulate gas, liquid or solid materials for ambient and vacuum condition experiments due to its high flexibility, mechanical tensile strength, and impermeability to small molecules (*18, 19*). In addition, graphene is also an excellent electrical and thermal conductor and displays minimal charging and heating effects under the electron beam (*17*). An inherently inert surface eliminates chemical and physical interference from the substrate. Here, we introduce the graphene liquid cell (GLC) as a real-time reaction chamber to study atom-resolved colloidal nanocrystal growth and dynamics with an aberration-corrected TEM.

The high-resolution liquid cell is prepared by encapsulating a Pt growth solution between two laminated graphene layers suspended over holes in a conventional TEM grid. An example of the GLC is illustrated in Figure 1: the TEM micrograph shows the encapsulated liquid sample (area with darker contrast) trapped between two suspended graphene sheets (lighter contrast) (Fig. 1(A)) accompanied with an idealized illustration (Fig. 1(B)). Graphene is grown on a copper foil substrate via chemical vapor deposition (CVD) (*20*) and then directly transferred onto a gold TEM mesh with a perforated amorphous carbon (a-C) support (*21*). We prepare a stock Pt growth solution by dissolving molecular Pt precursors ($Pt(acetylacetonate)_2$, 10 mg) in a mixture of *o*-dichlorobenzene and oleylamine (9:1 in volume ratio, 1 mL total) (*7*). The stock solution is pipetted directly atop two opposite-facing graphene-coated TEM grids (Fig. S1(A)). Upon wetting the system, the solution wicks between the graphene and a-C layers allowing one of the graphene membranes to detach from its associated TEM grid (*22*). Since the van der Waals

interaction between graphene sheets is relatively strong (*23*) liquid droplets of various thickness from 6-200 nm can be securely trapped between a double membrane liquid pocket or blister (Figs. 1, S1(B), and S2). Large surface strain imposed upon the detached graphene by the solution can also cause the edge of the graphene sheet to curl upon itself many times creating a nanoscroll, thus creating, if desired, multi-membrane protected liquid pockets (inset of Fig. S1(B)). Generally, for our GLCs graphene remains fully intact throughout the fabrication process as indicated by a relatively low defect-induced graphene D peak (around 1350 cm^{-1}) observed in Raman spectra (Fig. S3).

We image Pt nanocrystal growth and dynamics in as-prepared GLCs on the TEAM I (Transmission Electron Aberration-corrected Microscope I) managed by the National Center for Electron Microscopy. The microscope is operated at 80 kV with a beam intensity of 10^3 to 10^4 A/m^2 maintained during nanocrystal growth. Upon locating a liquid pocket on the TEM grid, the beam intensity is increased, which reduces the Pt precursor and initiates nanocrystal growth. (*7*). The graphene membrane with encapsulated liquid remains intact over the entire desired time period of TEM observation ensuring prolonged high-resolution *in-situ* imaging. Spherical and chromatic aberration correctors on TEAM I further contribute to the exceptionally high-resolution and enhanced signal-to-noise ratio (*24*).

Extended movies of colloidal Pt nanocrystal growth (S1 and S2) reveal major differences between data collected using GLCs compared to previous cells with silicon nitride windows (*7*) even at the earliest stages of the colloidal Pt nanocrystal growth. It is possible to clearly discern colloidal Pt nanoparticles as small as 0.1 nm radius and to track their motion. Using silicon nitride window cells, the nanoparticle motion is severely perturbed by the windows; nanoparticles of Au and Pt in such cells have been observed to remain localized close to one of the windows, weakly bound to the surface layer, and to execute complex non-Brownian motion near the window (*7, 25*). In contrast, the interaction of the nanoparticles with graphene is very

weak, and the motion of the colloidal Pt nanoparticles is not corrupted by association with the window. Two-dimensionally projected positions for a single nanocrystal trajectory are tracked in Movie S1 as it grows from 0.28 to 0.55 nm in radius by monomer attachment. As it grows, the particle diffusion slows as expected for Brownian motion (in the SiN cell the diffusivity does not scale this way due to substrate interactions). The trajectory is divided into three equal parts based on time. As the nanocrystal grows with time, the mean square displacement (MSD) $\langle x^2 \rangle$ decreases (Fig. 2A). Representative TEM images of the nanocrystal at each time frame are displayed in Fig. 2B with color gradient mapped images for clarification. The two-dimensional diffusivity D is extracted from the slope of the MSD as a function of time; the corresponding nanocrystal size is averaged for each time regime. Figure 2C shows that the measured D of a nanocrystal decreases monotonically as the nanocrystal steadily grows. One similarity with previous tracking studies in the silicon nitride window cells is that the nanocrystal diffusivities in the confined liquid are found to be smaller than those expected from the bulk liquid viscosity (*25*).

The nanocrystals grow both by monomer addition and by frequent coalescence events (Fig. S4). Using the GLC, it is possible to directly observe critically important features of the coalescence process that could not be resolved in earlier studies (TEM images of Pt nanocrystals in the final stage of the growth in GLCs can be found in Figs. S5 and S6). We first examine the crystallographic orientation relationship of nanocrystals during their coalescence. Figure 3 shows TEM images of *in-situ* Pt nanocrystal growth by coalescence. Incoming small nanocrystals are marked with white arrows on TEM images and can be seen clearly in black/white color mapped insets. Once nanocrystals collide at {111} planes, they merge quickly, within 0.26 seconds (the limit of our acquisition time). We observe that most coalescence events proceed along the same crystallographic direction indicating that there is a specific nanocrystal orientation for coalescence (Movie S2). This result is remarkable, since {111} planes of a face-centered cubic crystal have the lowest surface energy. This behavior may be due to different degrees of ligand

coverage on different nanocrystal factes; {111} planes of a face-centered cubic crystal have the lowest surface energy and therefore perhaps the lowest ligand coverage. In this scenario, nanocrystals that contact at {111} planes experience minimal ligand obstruction and therefore quickly unify to minimize the total surface area—and thus overall surface energy (*26*). Coalescence in this manner proceeds in one of two ways: contact which joins identical, or mirror, {111} planes. Nanocrystals captured in Fig. 3A exemplify the first instance, which results in a perfectly aligned crystal with a single crystallographic domain as shown in the fast-Fourier transformed (FFT) pattern. The second case, as seen in Fig. 2B and 2C yields nanocrystals with a twin boundary; the corresponding FFTs reveal two double domains. For the duration of our movies, twin boundaries formed from coalescence remain locked within the nanocrystal. The interface energy of the twin boundary is known to be thermodynamically non-negligible (*26*). However, it appears that, under the present experimental conditions, structural rearrangements of the nanoparticles occur mainly by surface rearrangements and not by reorganization of the complete nanocrystal interior. Mis-oriented particle coalescence appears to account for the formation mechanism of twin boundaries commonly observed in synthesized face-centered cubic metal nanocrystals (*26*).

Before coalescing along the {111} orientation, the nanocrystals exhibit a prolonged period of correlated motion that facilitates lattice alignment and unification. We track size (blue and green in Fig. 4A) and position change (Fig. 4B) of two nanocrystals before they coalesce at the sub-nanometer range. In Fig. 4A, two nanocrystals show correlated rather than independent motion over a 100 second interval, culminating in lattice alignment and coalescence. The correlated motion presumably arises because of inter-particle attractive forces. Based on theoretical studies, the attractive forces can be attributed to van der Waals interactions, steric repulsions, and depletion forces arising from surface ligands (*27*). The duration of the correlated motions we observe in Movies S1 and S2 vary depending on nanocrystal size and the local

thickness of the liquid medium. We measure the center-to-center distance (red in Fig. 4A) between two adjacent nanocrystals from a position plot of the two nanocrystals (Fig. 4B). Comparing this distance with nanocrystal size provides insight into the mechanisms of nanocrystal growth by coalescence. As the freely moving nanocrystals seen in Movie S1 draw close, the center-to-center distance rapidly decreases. This initial event occurs within 40 sec (see Fig. 4A). The center-to-center separation fluctuates between 4 to 6 nm for the next 25 sec. While this dynamic event proceeds, the nanocrystals also grow in size from around 0.75 nm to 1 nm in diameter due to monomer addition. The surface ligand, oleylamine, is known to be 1 to 2 nm long depending on the orientation and extension of its floppy alkyl chain and surface packing density (*28*). Therefore, the sustained correlated motion occurs with weakly touching surface ligand layers (*29*). The center-to-center distance shows even more confined fluctuation of about 1 nm in the time interval from 80 to 130 sec. In this time range we observe from Movie S1 and Fig. 4A that the correlated motion of the two nanocrystals exhibits three-dimensional behavior of rolling and relative sliding of nanocrystals over each other. Throughout this period the nanocrystals continue to grow by monomer addition, continuously increasing the attractive force between the particles. After 130 sec, the center-to-center distance approaches the sum of the radii of the two nanocrystals and the nanocrystals lattices align, leading to coalescence at 160 sec.

Single particle growth trajectories in the one previous lower-resolution study of Pt nanocrystal growth showed an apparent size decrease after coalescence, as well as a short pause following coalescence before apparent growth by monomer attachment has resumed (Fig. S4) (7). In the GLC, it is possible to examine and understand in much more detail these unexpected phenomena that follow nanoparticle coalescence. Figure 4C plots the change in length (l, along the center-to-center direction), thickness (t, vertical direction to the length), and neck diameter (n) of the coalesced nanocrystals, while Fig. 4D shows the corresponding TEM images. The nanocrystals are connected together by a neck at the initial stage of coalescence. Neck growth is

accompanied by a decrease in l and t. This indicates that the atoms migrate to the neck region by surface diffusion (*30*). Following coalescence, the nanocrystal structure also gradually reorganizes, evolving truncated surfaces. Returning to Fig. 3C, the nanocrystal shape after coalescence changes from quasi-spherical to a hexagonal shape that minimize the surface energy of nanocrystal as expected from a Wulff construction, also by surface diffusion processes.

The GLC has enabled the study of colloidal nanocrystal growth with unprecedented resolution, revealing a host of previously unexpected phenomena. We have directly observed the atomistic steps of nanocrystal coalescence and oriented attachment. The GLC introduced here can readily be applied to the study of diverse fluid samples including biological systems.

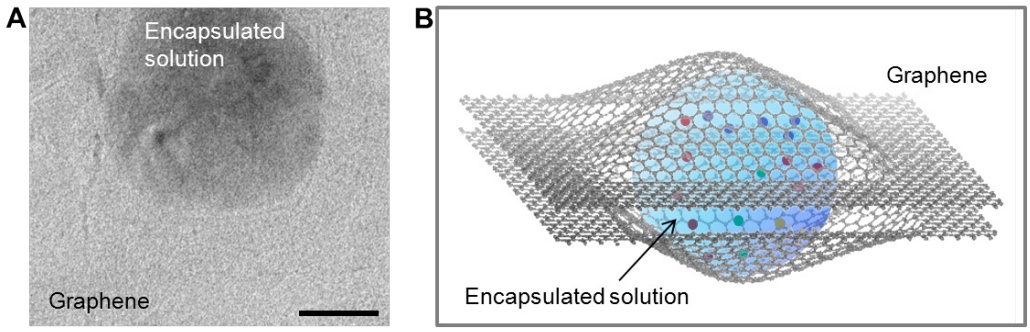

Figure 1. Graphene liquid cell (GLC). **(A)** TEM image of a GLC; laminated graphene layers immobilize a blister of encapsulated stock solution (dark region). Scale bar represents 50 nm. **(B)** Idealized illustration of local GLC encapsulating growth solution.

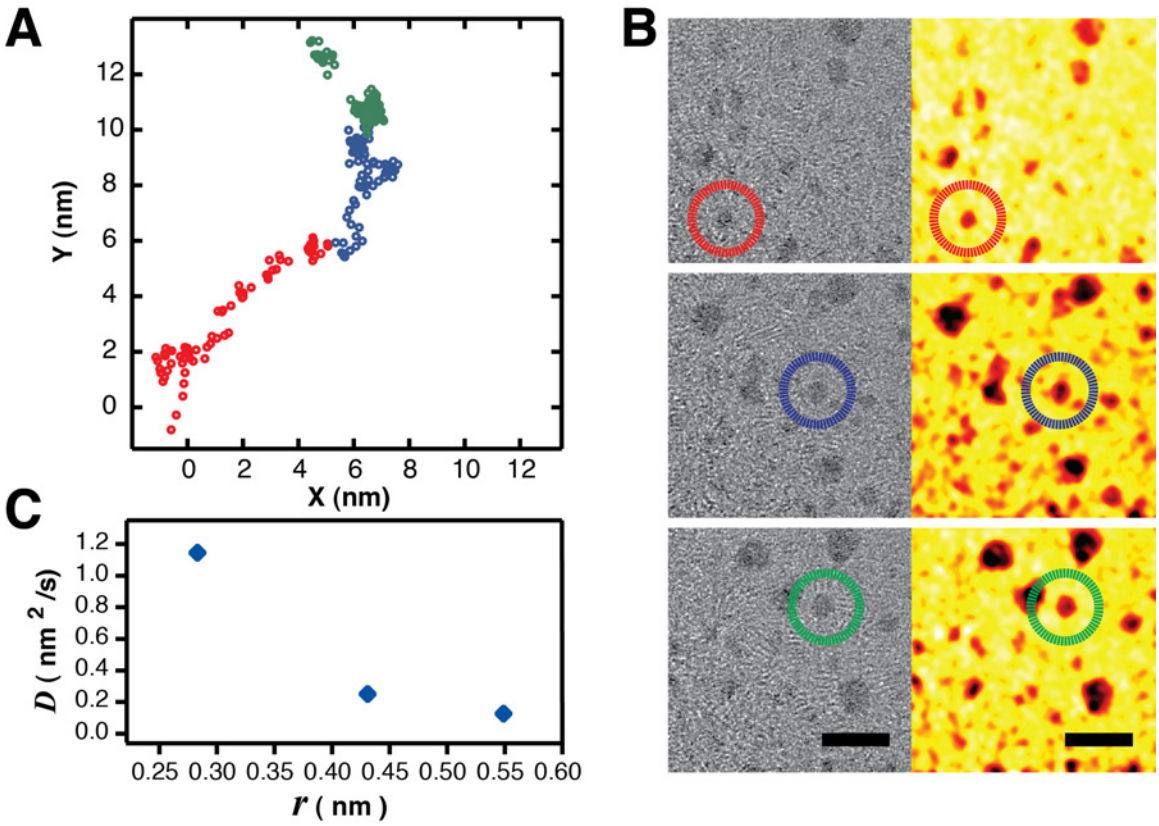

Figure 2. Tracking of nanocrystal position and measured diffusivity with average size from 0.28 nm to 0.55 nm in radius during growth. **(A)** Positions of a nanocrystal in consecutive time regimes of 20 seconds each during growth: red, blue, and green colors indicate the earliest to final time regime, respectively. **(B)** Representative TEM images from Movie S1 of the tracked nanocrystal in the different time regimes. Colors of the circles match the time regimes in (A). The panels on the right are false-color representations of the TEM contrast data. Scale bars represent 5 nm. **(C)** Diffusivity *D* as a function of average nanocrystal radius (*r*) over the 20 seconds of each regime.

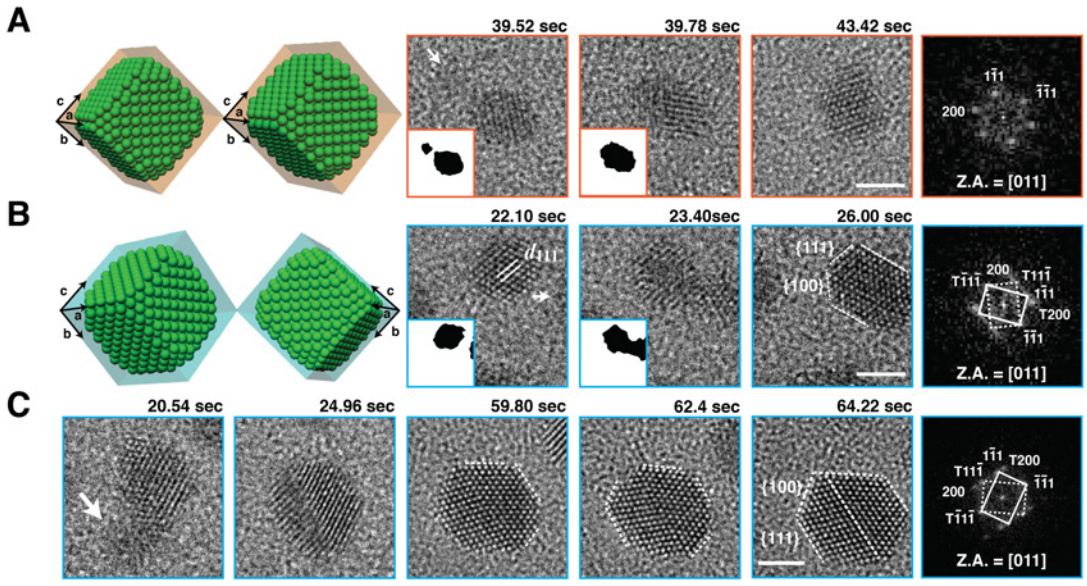

Figure 3. Still snapshots from Movie S2 of Pt nanocrystal growth via coalescence and crystal structure evolution observed with atomic resolution in a GLC. Schematic illustrations and corresponding TEM images exhibiting nanocrystal coalescence along <111> directions which evolve into **(A)** a single crystalline face-centered cubic structure or **(B)** a twinned face-centered cubic structure. Black and white insets represent scaled down nanocrystal volume projections and background, respectively, to clarify the nanocrystal shapes and positions. **(C)** Shape evolution of the Pt nanocrystal by straightening of the twin boundary and evolution towards a hexagonal shape consistent with the Wulff construction. These reconstructions are consistent with surface rearrangements. For (A)-(C), FFT images of the final frame are provided at the end of each sequence. Arrows point out incoming nanocrystals. Scale bars are 2 nm and zone axis abbreviated as Z.A.

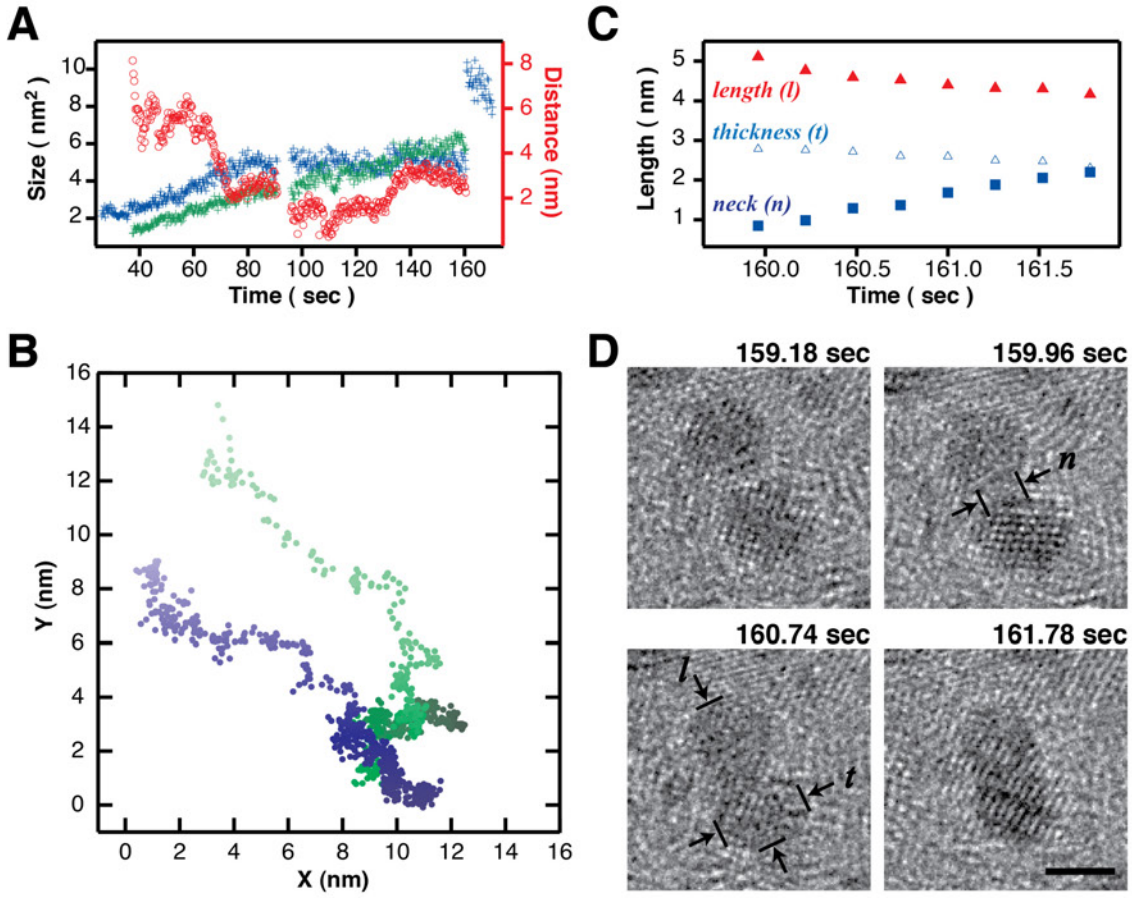

Figure 4. Pt nanocrystal dynamics before (A, B) and after coalescence (C, D). **(A)** Projected distance between two nanocrystals (red) up until the two nanocrystals coalesce, as well as the size (blue and green, area (nm^2) is measured for spherical and ellipsoidal nanocrystal shapes before and after coalescence, respectively) of the two nanocrystals during the period of correlated motion. The nanocrystal labeled in green merges with the blue-labeled nanocrystal at 160 sec. Structural reorganization is tracked with atomic resolution after the coalescence event. (Two consecutive movie clips were merged into Movie S1, accounting for the data gap of 5 sec at the 95 sec point.) **(B)** Two-dimensional projected position change of the two nanocrystals before coalescence. Blue and green colors correspond to the nanocrystals in (A). Color gradient is used to represent time eolution from 40 sec (bright color) to 160 sec (dark color). **(C)** Neck diameter (*n*), thickness (*t*), and length (*l*) after the coalescence of the two nanocrystals as a function of time. Time domain of this plot corresponds to the interval the apparent nanocrystal size decreases after

coalescence in (A). **(D)** Still snapshots from Movie S1 showing neck formation during coalescence and shape evolution into an ellipsoid by neck filling and length reduction of the nanocrystal. Scale bar represents 2 nm.

References

1. J. C. Meyer, C. O. Girit, M. F. Crommie, A. Zettl, *Nature* **454**, 319 (2008).
2. C. –Y. Wen, M. C. Reuter, J. Bruley, J. Tersoff, S. Kodambaka, E. A. Stach, F. M. Ross, *Scien ce*, **326**, 1247 (2009).
3. V. Radmilovic *et al.*, *Nature Mater*. **10**, 710 (2011).
4. A. H. Zewail, *Science* **328**, 187 (2008).
5. N. de Jonge, F. M. Ross, *Nature Nanotech.* **6**, 695 (2011).
6. M. J. Williamson, R. M. Tromp, P. M. Vereecken, R. Hull, F. M. Ross, *Nature Mater.* **2**, 532 (2003).
7. H. Zheng *et al.*, *Science* **324**, 1309 (2009).
8. J. E. Evans, K. L. Jungjohann, N. D. Browning, I. Arslan, *Nano Lett.* **11**, 2809 (2011).
9. K. S. Novoselov *et al.*, *Proc. Natl. Acad. Sci.* **102**, 10451 (2005).
10. X. Li *et al.*, *Nature Nanotech.* **3**, 538 (2008).
11. J. N. Coleman *et al.*, *Science* **331**, 568 (2011).
12. Z. Lee *et al.*, *Nano Lett*. **9**, 3365 (2009).
13. A. Kolmakov *et al.*, *Nature Nanotech.* **6**, 651 (2011).
14. Y. A. Wu *et al.*, *Nanotechnology* **22**, 195603 (2011).
15. J. C. Meyer, C. O. Girit, M. F. Crommie, A. Zettl, *Appl. Phys. Lett.* **92**, 123110 (2008).
16. R. Erni *et al.*, *Phys. Rev. B* **82**, 165443 (2010).
17. R. R. Nair *et al.*, *Appl. Phys. Lett.* **97**, 153102 (2010).
18. J. M. Yuk *et al.*, *Nano Lett.* **11**, 3290 (2011).
19. K. Xu, P. Cao, J. R. Heath, *Science* **329**, 1188 (2010).
20. X. Li *et al.*, *Science* **324**, 1312-1314 (2009).
21. W. Regan *et al.*, *Appl. Phys. Lett.* **96**, 113102 (2010).

22. X. Xie *et al.*, *Nano Lett.* **9**, 2565 (2009).

23. S. P. Koenig, N. G. Boddeti, M. L. Dunn, J. S. Bunch, *Nature Nanotech.* **6**, 543 (2011)

24. E. A. Stach, *Mater. Today* **11**, 50 (2008).

25. H. Zheng, S. A. Claridge, A M. Minor, A. P. Alivisatos, U. Dahmen, *Nano Lett*. **9**, 2460 (200 9).

26. X. Lu, M. Rycenga, S. E. Skrabalak, B. Wiley, Y. Xia, *Annu. Rev. Phys. Chem.* **60**, 167 (2009) .

27. K. J. M. Bishop, C. E. Wilmer, S. Soh, B. A. Grzybowski, *Small* **5**, 1600 (2009).

28. X. Lu, M. S. Yavuz, H. –Y. Tuan, B. A. Korgel, Y. Xia, *J. Am. Chem. Soc.* **130**, 8900 (2008).

29. P. Schapotschnikow, R. Pool, T. J. H. Vlugt, *Nano Lett.* **8**, 2930 (2008).

30. Z. Z. Fang, H. Wang, *Int. Mater. Rev.* **53**, 326 (2008).

Acknowledgement

Work on preparation of a nanocrystal growth solution, portions of the design and construction of GLC, and data analysis was support by the Physical Chemistry of Inorganic Nanostructures Project, KC3103, Director, Office of Science, Office of Basic Energy Sciences, of the United States Department of Energy under contract DE-AC02-05CH11231. Portions of the present study were performed at the National Center for Electron Microscopy, Lawrence Berkeley National Laboratory, which is supported by the U.S. Department of Energy under contract no. DE-AC02-05CH11231. J.M.Y. and J.Y.L. acknowledge the financial support from Priority Research Centers Program through the National Research Foundation of Korea (NRF) funded by the Ministry of Education, Science and Technology (Grant No. 2010-0029714). A.Z. acknowledges support from the Director, Office of Energy Research, Office of Basic Energy Sciences, Materials Sciences and Engineering Division, of the US Department of Energy under contract DE-AC02-05CH11231, which provided for the design and construction of the GLC, and support from the Office of Naval Research under Grant N00014-09-1-1066 which provided for graphene growth and spectral characterization. K.K. received further support from the National Science Foundation, Grant EEC-0832819, for preliminary TEM imaging and analysis

necessarily constitute or imply its endorsement, recommendation, or favoring by the United States Government or any agency thereof, or The Regents of the University of California. The views and opinions of authors expressed herein do not necessarily state or reflect those of the United States Government or any agency thereof or The Regents of the University of California.

Supporting Online Material

Supporting Online Material for

High-Resolution Transmission Electron Microscopy Observation of Colloidal Nanocrystal Growth Mechanisms using Graphene Liquid Cells

Jong Min Yuk,[1,2,3]* Jungwon Park,[2,4]* Peter Ercius,[5] Kwanpyo Kim,[1,2,6] Danny J. Hellebusch,[2,4] Michael F. Crommie,[1,2,6] Jeong Yong Lee,[3]† A. Zettl,[1,2,6]† A. Paul Alivisatos[2,4]†

[1] Department of Physics, University of California at Berkeley, CA 94720, USA.

[2] Materials Sciences Division, Lawrence Berkeley National Laboratory, Berkeley, CA 94720, USA.

[3] Department of Materials Science and Engineering, KAIST, Daejeon 305-701, Korea.

[4] Department of Chemistry, University of California at Berkeley, CA 94720, USA.

[5] National Center for Electron Microscopy, Lawrence Berkeley National Laboratory, Berkeley, CA 94720, USA.

[6] Center of Integrated Nanomechanical Systems, University of California at Berkeley, CA 94720, USA.

*These authors contributed equally to this paper.

†To whom correspondence should be addressed: j.y.lee@kaist.ac.kr; azettl@berkeley.edu; and alivis@berkeley.edu

S1. Supporting Movie Legends

Growth dynamics of platinum nanocrystals in a graphene liquid cell observed *in-situ* using a TEAM I. A growth solution of Pt(acetylacetonate)$_2$ (10 mg/mL) in a mixture of *o*-dichlorobenzene and oleylamine (9:1 in volume ratio) was used. The growth of platinum nanocrystals was initiated by electron beam irradiation. During 5 seconds of electron beam illumination, liquid was too thick to detect nanocrystal motions. Thereafter, the liquid thickness became thin enough to observe nanocrystal motions in the area of electron beam illumination, a consequence of the electron beam inducing thinning in the liquid by knock-on damage.

Movie S1. This movie shows diffusion and coalescence of nanocrystals. The frame rate is ~3.85/sec. Two movies were taken back-to-back with a dead time of 5 seconds between them; they were combined for Movie S1. The dead time is seen as a gap data in Fig. 4A.

Movie S2. This movie shows diffusion, oriented attachment, and faceting of nanocrystals. The frame rate is ~ 3.85/sec.

S2. Methods

Microscopy. The low magnification TEM imaging was performed in a JEM-2010 LaB_6 instrument (JEOL Ltd.) at 100 kV.

High-resolution TEM images were acquired with the TEAM 1 operated at 80kV at the National Center for Electron Microscopy. This electron microscope has a high-brightness gun (X-FEG) and probe as well as image and chromatic aberration correctors. The image corrector (C_s) was fine tuned to obtain a third-order spherical aberration of −10μm, which in consideration of the positive fifth-order aberration (C_5) of 2.5 mm yielded optimal phase contrast with slight positive defocus. The theoretical information limit of 0.05 nm can thus be achieved at 80 kV. The resulting electron dose is approximately 4×10^5 e^-/sec·nm^2. We set 0.03 seconds of exposure time,

0.23 seconds of read out time, and therefore 0.26 seconds of entire frame time to acquire time-serial images. More details of the microscope configuration can be found elsewhere [S1].

AFM images were taken on a MFP-3D scanning probe microscope (Asylum Research instruments). AFM imaging was performed on suspended GLC samples on Quantifoil TEM grids in non-contact mode using a V-shaped 'NSC35' probe C (phosphorus-doped Si with frequency f_c = 150 kHz, spring constants k = 4.5 N m^{-1}, and nominal tip radius 10 nm). All images were collected under ambient conditions at 23 °C with a scanning rate of 2.5-10 um/s.

SEM images were performed using FEI XL3000 at 5 kV.

Spectroscopy. The Raman measurements were performed using Renishaw inVia Raman microscope with 514 nm Ar ion laser.

S3. Supporting Figures and Legends

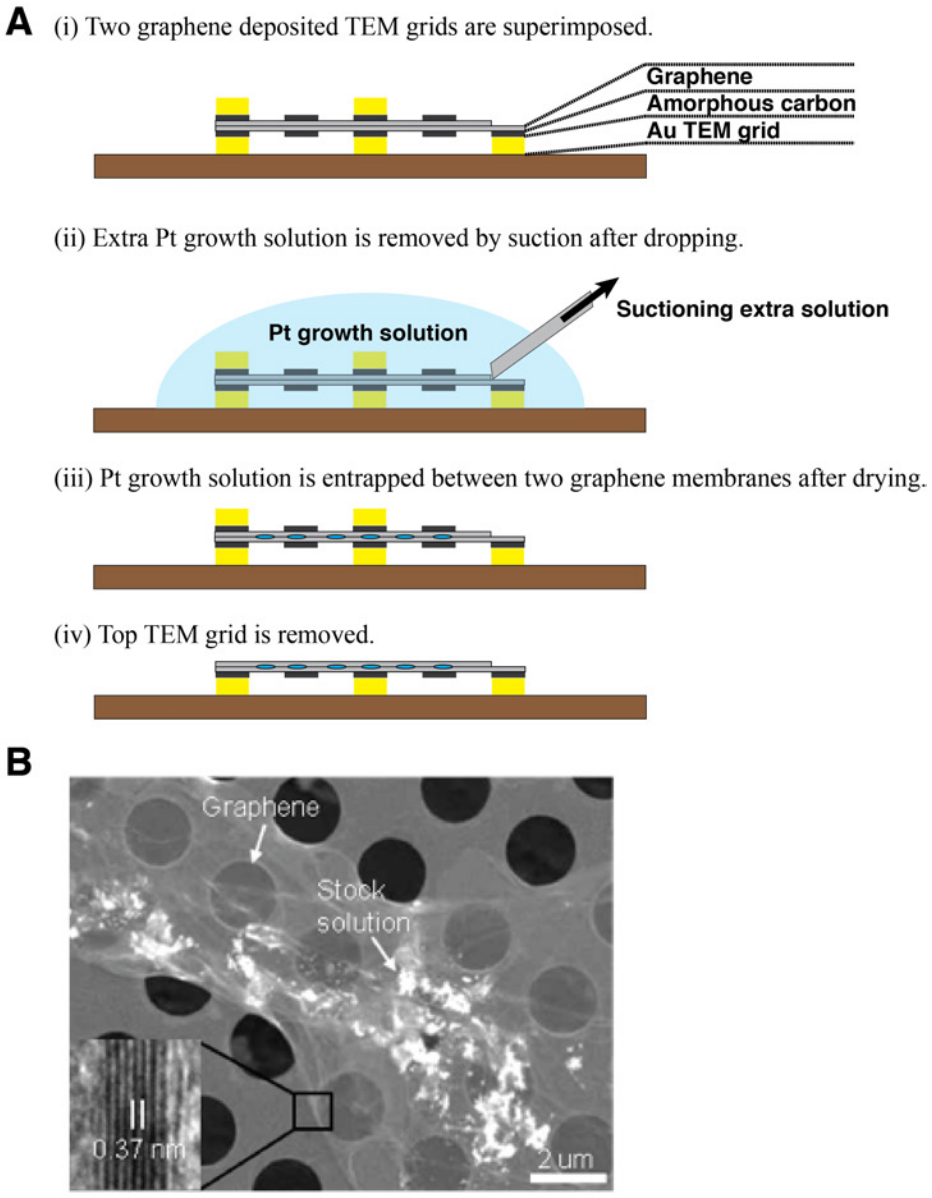

Fig. S1. Preparation of a graphene liquid cell. **(A)** Illustration of the fabrication processes of the graphene liquid cell. **(B)** SEM image of a graphene liquid cell. The inset is a TEM image of a nine-layered graphene on edge; that the distance between adjacent graphene layers is 0.37 nm.

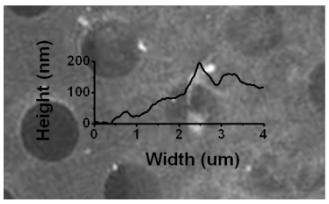

Fig. S2. AFM image and height profile of a GLC supported on a holey a-C grid. Encapsulated Pt growth solution appears white in the image and yields a spike in the height profile.

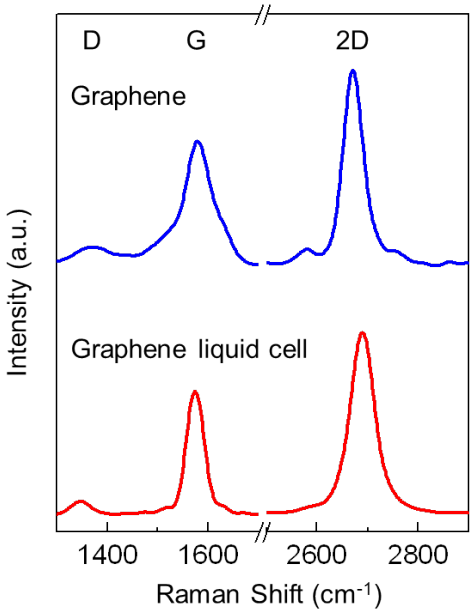

Fig. S3. Raman spectra of graphene deposited on TEM grid and graphene liquid cell.

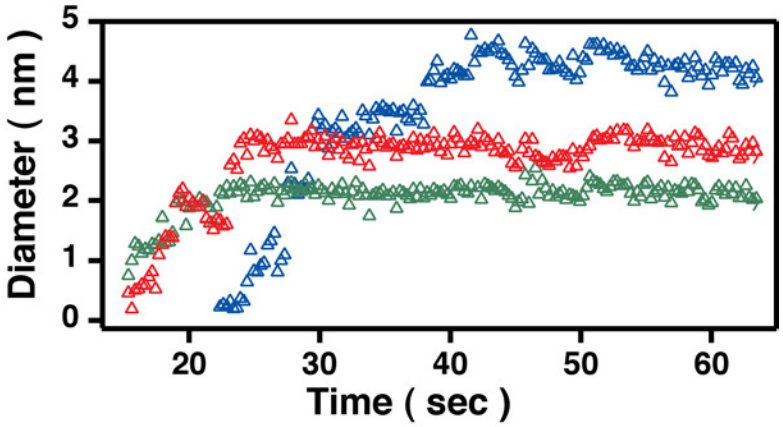

Fig. S4. Growth trajectories of individual Pt nanocrystal in several pathways: gradual growth by monomer addition, green; a single coalescence, red; and multiple coalescence, blue.

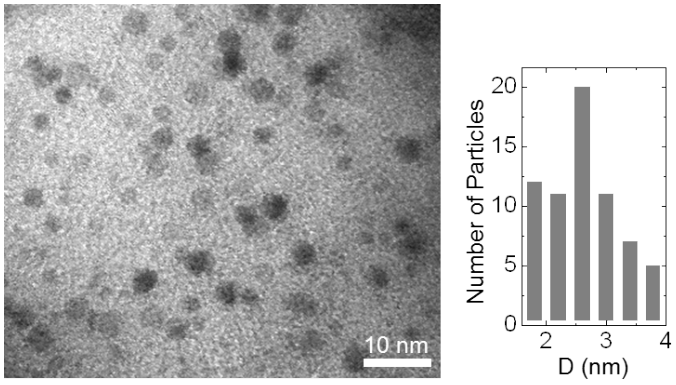

Fig. S5. Bright-field TEM image of Pt nanocrystals synthesized in a graphene liquid cell by the exposure of the growth solution to the electron beam for about 5 min and with corresponding particle diameter (D) histogram.

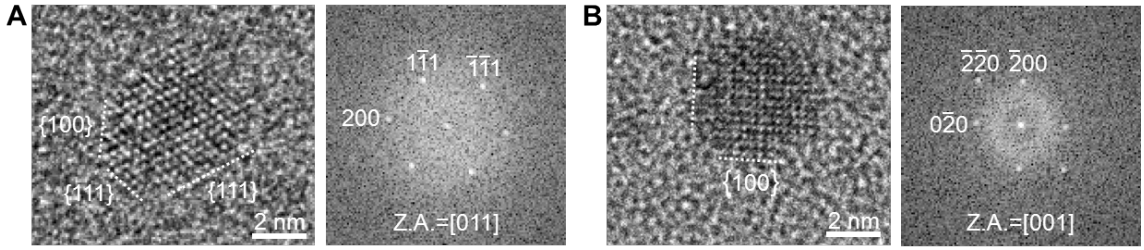

Fig. S6. High-resolution TEM images and FFT patterns of Pt nanocrystals **(A)** along the [011] zone axis (Z.A.) showing {100} and {111} facets and **(B)** along the [001] direction showing {100} facets.

References

S1. Available at http://ncem.lbl.gov/TEAM-project/index.html.